Received: 1 February 2019 | Revised: 14 May 2019 | Accepted: 18 July 2019

DOI: 10.1002/aic.16732

Comparison of Eulerian QBMM and classical Eulerian–Eulerian method for the simulation of polydisperse bubbly flows

Dongyue Li[1,2] | Daniele Marchisio[3] | Christian Hasse[4] | Dirk Lucas[2]

[1]State Key Laboratory of Advanced Metallurgy, University of Science and Technology, Beijing, China

[2]Helmholtz-Zentrum Dresden-Rossendorf, Dresden, Germany

[3]Politecnico di Torino, Torino, Italy

[4]Institute for Simulation of Reactive Thermo-Fluid Systems, Technische Universität Darmstadt, Darmstadt, Germany

Correspondence
Daniele Marchisio, Politecnico di Torino, Torino 10129, Italy.
Email: daniele.marchisio@polito.it

Dongyue Li, State Key Laboratory of Advanced Metallurgy, University of Science and Technology, Beijing 100083, China.
Email: li.dy@dyfluid.com

Funding information
Helmholtz-Zentrum Dresden-Rossendorf
Open access funding enabled and organized by Projekt DEAL
[Correction updated on 31 October 2020 after first online publication.]

Abstract

The spatial gas distribution of poly-disperse bubbly flows depends greatly on the bubble size. To reflect the resulting polycelerity, more than two momentum balance equations (typically for the gas and liquid phases) have to be considered, as done in the multifluid approach. The inhomogeneous multiple-size group model follows this approach, also combined with a population balance model. As an alternative, in a previous work, an Eulerian quadrature-based moments method (E-QBMM) was implemented in OpenFOAM; however, only the drag force was included. In this work, different nondrag forces (lift, wall lubrication, and turbulent dispersion) are added to enable more complex test cases to be simulated. Simulation results obtained using E-QBMM are compared with the classical E–E method and validated against experimental data for different test cases. The results show that there is good agreement between E-QBMM and E–E methods for mono-disperse cases, but E-QBMM can better simulate the separation and segregation of small and large bubbles.

KEYWORDS
bubbly flow, E–E method, E-QBMM, non-drag forces, wall peak

1 | INTRODUCTION

Bubbly flows are relevant in many applications belonging to various industries such as chemicals, pharmaceutics, food and power production, among others. The prediction of the gas phase (bubble) distribution is of paramount importance for designing apparatus and optimizing processes. Many experimental studies have been published showing that interfacial forces, such as drag, lift, wall lubrication, and turbulent dispersion forces, are important under the bubbly flow regime.[1-3] The drag force considers the resistance between the phases and, together with buoyancy, determines the bubble's terminal velocity. The lift force is related to the velocity gradient in the continuous phase and acts laterally to the bubble motion. It may change its sign depending on the bubble size, as the lift force experienced by small spherical bubbles differs from that experienced by large ellipsoidal ones. In upward bubble flows, the lift force pushes the small bubbles toward the wall and the large bubbles toward the center of the pipe. The wall lubrication force prevents bubbles from collecting at the wall. Moreover, the turbulent dispersion force considers the bubble dispersion due to the effect of turbulent eddies. It is proportional to the gas volume fraction gradient and flattens the corresponding profiles. It has been shown to improve the stability of the E–E method.[4]

As shown in Figure 1, all these forces have an effect on the bubbles' migration, and as a result the profile of the phase fraction distribution is established as the outcome of multiple factors. In particular, when only the drag force is included, all the bubbles move upward with negligible radial migration. The predicted phase fraction is flattened somewhat, since no lateral forces are exerted. If the lift force is included, the small bubbles tend to move toward the wall forming a gas volume fraction profile with a maximum directly at the wall. If the wall lubrication force is also included, the predicted phase fraction profile exhibits a peak next to the wall, since the wall lubrication force pushes the bubbles away from the wall. When in addition the

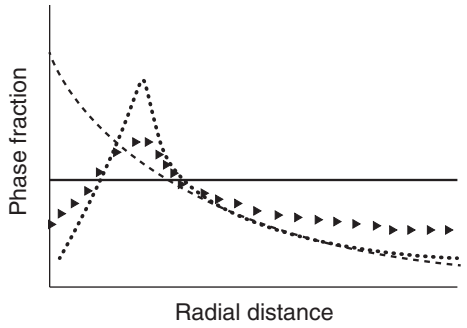

FIGURE 1 Typical phase fraction profile predicted by CFD for small bubbles (e.g., d < 5 mm) in vertical upward pipe. Solid line: Only drag force. Dashed line: Drag + lift force. Dots: Drag + lift + wall lubrication force. Triangles: Drag + lift + wall lubrication + turbulent dispersion force

TABLE 1 Different PBM solving methods

PBE solving method	References
Quadrature method of moments (QMOM)	Mcgraw[30]
Multiple-size group (MUSIG) method	Lo[31]
Least-square method	Dorao and Jakobsen[32]
Fixed-pivot method	Kumar and Ramkrishna[33]

turbulence dispersion model is considered, the phase fraction profile is flattened, since it acts as a diffusion term. It should be noted here that the statement above is quite general. For example, whether the wall lubrication model developed by Hosokawa et al [5] or Antal et al [6] is used, the predicted phase fraction exhibits similar resulting features with a wall peak. Besides the phase fraction distribution, the gas holdup is also important. However, the consideration of the column aspect ratio and its influence on the holdup concerns global parameter. The investigation of critical values is not the objective of this work. Readers are referred to other works for more information.[7-10]

Thanks to increasing computational power, computational fluid dynamics (CFD) methods have become more and more feasible as a means of examining such complex flows. The macroscopic Eulerian–Eulerian (E–E) method has been employed extensively to investigate bubbly flows in many studies.[11-17] However, one drawback of the classical two-phase E–E method is that it can only be employed for monodisperse systems. Here, mono-dispersity refers to situations in which all the bubbles have the same properties (e.g., bubbles with identical diameters). In contrast, poly-dispersity refers to situations in which the properties of the disperse-phase entities are different for each entity (e.g., bubbles with different diameters). In practice, mono-disperse bubbly flows are relatively rare, hence, it will be important to have a modeling framework that naturally accounts for poly-dispersity. In order to extend the method to include poly-disperse systems and to allow for the consideration of bubble coalescence and breakup, CFD was coupled with population balance models and employed to simulate poly-disperse systems.[18-24] In the CFD-PBM coupling procedure, the mean Sauter diameter is calculated by the PBM and fed into the momentum interfacial exchange terms. Table 1 shows the different PBM solving methods. Readers interested in this subject are referred to another recent work.[25] These methods are valid only for small Stokes flows (e.g., liquid–liquid emulsions with relatively homogeneous droplet diameters) since the disperse phase is still convected by one velocity field for all bubble or droplet sizes.[26] However, many experimental studies on polydisperse bubbly flows have shown that, when polydispersity is significant, bubbles tend to migrate at different velocities depending on their size. These effects are caused by the fact that interfacial forces depend on the bubble size; this is particularly important for the lift force, where the inversion of sign of the lateral lift force in vertical upward bubbly flows even causes small and large bubbles move toward opposite directions.[27-29]

To predict such polydisperse multiphase flows, CFD-PBM coupling was extended to include other multiphase E–E methods, in which bubbles within a range of sizes are handled as separate phases (the inhomogeneous multiple-size group [MUSIG] model).[34-36] Another solution is to systematically couple the CFD with a more general PBM, based on the so-called generalized population balance equation (GPBE), in which Navier–Stokes equations are employed for the continuous phase, while the GPBE is employed for the disperse phase. The GPBE operates based on a number density function (NDF) that completely defines the polydispersity of the system. In this procedure, the GPBE is transformed into a set of transport equations for the moments of the NDF, which are in turn solved numerically using the finite volume method (FVM), as are all the other governing equations of the CFD model. This method is also labeled "Eulerian QBMM" with "Eulerian" referring to the approach for the continuous phase and "QBMM" denoting the quadrature-based moments method. In fact, the transport equations for the moments of the NDF are closed using a quadrature approximation. To model the phase velocity of the disperse phase, different methods can be chosen, such as the conditional quadrature method of moments (CQMOM) [37] or the velocity polynomial approximation (VPA) model.[38-40] In CQMOM, the disperse phase velocity is treated as a separate "internal coordinate," and the quadrature approximation is used to overcome the closure problem. The quadrature approximation consists of different abscissas or nodes that can be thought of as separate bubble classes or "phases." This approach was mainly used to predict particle trajectory crossing. In the VPA model, by contrast, the disperse phase velocity is not formally treated as an independent internal coordinate, and a polynomial relationship is assumed between the bubble velocity and bubble size.

In this work, we implemented the full set of interfacial momentum exchange terms in the E-QBMM and validated the algorithm with experimental data. Specifically, nondrag forces are implemented and their effects on bubble separation are shown and compared with the two-phase E–E method. Experimental data taken from the literature on bubbly flow in pipes resulting in various gas phase radial and axial distributions were included to validate the algorithm and its implementation. Model predictions are validated against three upward vertical pipe flow experiments investigated by Žun,[41] Banowski et al,[29] and Lucas et al,[42] which operated at different geometries and different superficial velocities. The first two test cases feature the double peak phase fraction distribution, which corresponds to the polydisperse systems. The last one features the wall peak distribution, which

corresponds to the monodisperse systems. Our results show that the wall peak predicted by the fully coupled E-QBMM with a full set of the momentum interfacial exchange terms is identical to that predicted using the E–E method. On the other hand, E-QBMM is also capable of predicting the double peak phase fraction distribution for poly-disperse systems, since the bubbles of different sizes are transported at different velocities by the VPA; the predictions agree well with experimental data.

2 | MODEL DESCRIPTION AND NUMERICAL DISCRETIZATION

2.1 | Eulerian method for the continuous phase

In the absence of mass transfer between phases, the mass conservation equation and the momentum balance equation for the continuous phase is described by

$$\frac{\partial(\alpha_c\rho_c)}{\partial t} + \nabla\cdot(\alpha_c\rho_c\mathbf{U}_c) = 0, \tag{1}$$

$$\frac{\partial(\alpha_c\rho_c\mathbf{U}_c)}{\partial t} + \nabla\cdot(\alpha_c\rho_c(\mathbf{U}_c\otimes\mathbf{U}_c)) - \nabla\cdot(\alpha_c\rho_c\mathbf{R}_c) = \alpha_c\nabla p + \alpha_c\rho_c\mathbf{g} - \mathbf{A}, \tag{2}$$

where α_c is the phase fraction of the continuous phase, ρ_c is its density, and $\mathbf{U}_c$ is its average velocity, $\mathbf{R}_c$ represents the stress tensor, p is the average pressure, $\mathbf{g}$ is the gravity acceleration vector, and $\mathbf{A}$ is the momentum interface exchange term, which will be discussed in the next section.

2.2 | GPBE/QBMM for the disperse phase

Considering the NDF $n(t, \mathbf{x}, d, \mathbf{V}_d)$, the GPBE for the disperse phase can be written as [38]

$$\frac{\partial n}{\partial t} + \nabla_{\mathbf{x}}\cdot(\mathbf{V}_d n) + \nabla_{\mathbf{V}_d}\cdot(\mathbf{A}n) = S, \tag{3}$$

where $\mathbf{V}_d$ is the bubble velocities, S is the possible source term, which is neglected in this work, $\mathbf{A}$ is the continuous rate of change of particle velocity, or the force per unit mass acting on bubbles (e.g., drag, lift, etc.), which generally depends on $\mathbf{V}_d$. Equation 3 can be solved by a direct solver, such as the direct simulation Monte Carlo (DSMC) method and others, with additional computational cost. Alternatively, some approximations can be also made. In this work, we employ VPA. It assumed that the velocity of the elements of the disperse phase depends on size. A suitable approximation is to use a second-order polynomial:[38]

$$\mathbf{V}(d) = \mathbf{P}_0 + \mathbf{P}_1 d + \mathbf{P}_2 d^2, \tag{4}$$

where d is the particle size and $\mathbf{P}_i$ are the velocity polynomial coefficients (VPCs). Equation 4 can be written in the following expanded form:

$$\begin{aligned} v_x(d) &= p_{0,x} + p_{1,x}d + p_{2,x}d^2, \\ v_y(d) &= p_{0,y} + p_{1,y}d + p_{2,y}d^2, \\ v_z(d) &= p_{0,z} + p_{1,z}d + p_{2,z}d^2, \end{aligned} \tag{5}$$

where v_x, v_y, v_z are the velocity components in the Cartesian coordinate system and $p_{i,x}$, $p_{i,y}$, and $p_{i,z}$ are the components of $\mathbf{P}_i$. Once the VPCs are determined, the conditional particle velocities $\mathbf{V}(d)$ can be updated from the particle size.

To solve Equation 3 numerically with the VPA, the operator splitting procedure is employed in this work.[38] In the first step of operator splitting, only convection is considered:

$$\frac{\partial n}{\partial t} + \frac{\partial v_x n}{\partial x} + \frac{\partial v_y n}{\partial y} + \frac{\partial v_z n}{\partial z} = 0. \tag{6}$$

This equation can be transformed into the mixed-moments transport equations

$$\frac{\partial m_{j,k,l,i}}{\partial t} + \frac{\partial m_{j+1,k,l,i}}{\partial x} + \frac{\partial m_{j,k+1,l,i}}{\partial y} + \frac{\partial m_{j,k,l+1,i}}{\partial z} = 0 \tag{7}$$

by defining of the mixed moments of the NDF:

$$m_{j,k,l,i} = \int v_x^j v_y^k v_z^l d^i \mathrm{d}u\mathrm{d}v\mathrm{d}w\mathrm{d}d. \tag{8}$$

When $m_{j,k,l,i}$ in Equation 7 are solved, $m_{j+1,k,l,i}$, $m_{j,k+1,l,i}$, and $m_{j,k,l+1,i}$ need to be known, which implies that Equation 7 is not closed. In this work, it is closed using a quadrature approximation, as formulated in the original quadrature method of moments,[30] in which any higher order mixed moment can be calculated as

$$m_{j,k,l,i} = \sum_{\beta=1}^{N} w_\beta v_x(d_\beta)^j v_y(d_\beta)^k v_z(d_\beta)^l d_\beta^i, \tag{9}$$

where w_β and d_β are the weights and abscissas of the quadrature approximation calculated from the pure moments of the NDF with respect to bubble size, N is the number of nodes, $v_x(d_\beta)$, $v_y(d_\beta)$, $v_z(d_\beta)$ are the three components of the bubble velocity and an assumption is made on the dependence of bubble velocity versus bubble size. The N weights and abscissas can be calculated from the first 2 N moments using the moment inversion algorithm (e.g., the Wheeler algorithm).[43] The calculation is done using only the first 2 N moments of the NDF with respect to bubble size $m_{0,0,0,i}$ with i = 0,1,…2 N−1. Moreover, the velocity polynomial coefficients $\mathbf{P}_i$ with i = 0, 1, 2 as defined in Equation 4 can be calculated from the pure moments of the NDF with respect to bubble size $m_{0,0,0,i}$ by constructing a moment matrix system. Then the higher order mixed moments can be calculated based on Equation 9 and Equation 5, and Equation 7 can be solved using the higher order realizable FVM.[44] Readers interested in the details of the first step of the operator splitting procedure are invited to refer to our previous work.[40]

After the convection terms are updated (the second term on the R.H.S of Equation 3) in operator splitting procedure step 1, the effect

of the force term (the third term on the R.H.S of Equation 3) on the disperse phase velocity needs to be considered. This constitutes the operator splitting procedure step 2. Because the forces only affect the velocities, the velocities can be updated with the following ordinary differential equation (ODE):

$$\alpha_\beta \frac{d\mathbf{V}_\beta}{dt} = \mathbf{A}_{\beta,\text{buo}} + \mathbf{A}_{\beta,\text{drag}} + \mathbf{A}_{\beta,\text{lift}} + \mathbf{A}_{\beta,\text{wall}} + \mathbf{A}_{\beta,\text{bubblePres}}, \quad (10)$$

where α_β is the phase fraction of the disperse phase with abscissas (particle size) d_β, $\mathbf{A}_{\beta,\text{ buo}}$ denotes the buoyancy force, $\mathbf{A}_{\beta,\text{ drag}}$ denotes the drag force, $\mathbf{A}_{\beta,\text{ lift}}$ denotes the lift force, $\mathbf{A}_{\beta,\text{ wall}}$ denotes the wall lubrication force, and $\mathbf{A}_{\beta,\text{ bubblePres}}$ denotes the bubble pressure force. The buoyancy force can be modelled as

$$\mathbf{A}_{\beta,\text{buo}} = \alpha_\beta \mathbf{g}\left(1 - \frac{\rho_c}{\rho_\beta}\right), \quad (11)$$

in which $\mathbf{g}$ is the gravity acceleration vector and ρ_β is the density of the disperse phase with size d_β. For the bubbly pipe flows investigated in this work, the buoyant force acting on the radial direction accelerates the bubbles' upward movement. The drag force can instead be modeled as

$$\mathbf{A}_{\beta,\text{drag}} = \alpha_\beta \frac{3 C_{D,\beta}\rho_c}{4 d_\beta} |\mathbf{U}_c - \mathbf{V}_\beta| (\mathbf{U}_c - \mathbf{V}_\beta), \quad (12)$$

In vertical upward bubbly flows, the drag force counterbalances the buoyancy force and this determines bubble's terminal velocity.

The lift force plays a critical role in the prediction of the lateral behavior of bubbly flows. Therefore, a correct description of the lift coefficient in bubble columns is crucial in order to model this transversal force correctly. It can be calculated by the following expression:

$$\mathbf{A}_{\beta,\text{lift}} = \alpha_\beta C_{L,\beta} \frac{\rho_c}{\rho_\beta}(\mathbf{U}_c - \mathbf{V}_\beta) \times (\nabla \times \mathbf{U}_c), \quad (13)$$

where $C_{L,\,\beta}$ is the lift force coefficient, which can be calculated by different models.[27] The main feature of the lift force is that the model is capable of predicting the so-called cross-over point, at which bubble distortion causes a reversal in the sign of the lift force. The coefficient $C_{L,\,\beta}$ becomes negative for large bubbles (e.g., for air bubbles in pure water larger than 5.6 mm), largely affecting the dynamics of bubble radial and axial redistribution in horizontal pipes. It should be noted that the critical value at which the sign of $C_{L,\,\beta}$ changes may differ slightly. It depends mainly on the shape and dimension of the bubble. Besagni and Inzoli [45] found that the bubble aspect ratio depends on the bubble size in bubbly flows. Spherical bubbles are relatively rare compared with ellipsoidal bubbles. Different models have been proposed to model the bubble aspect ratio.[45,46] Recently new measurements on the lift force for air-water flows were done, and the effect of the bubble shape was discussed.[47] The validity of the change of the sign of the lift force in dependence on the bubble size was also shown for ploy-disperse flows turbulent flows.[28,47] There might be some limits for highly turbulent flows. However, the proper correlation for the evaluation of the lift force is still controversial. Some authors claim that the intensity of turbulent fluctuations also plays an important role, but most researchers agree that bubbles of different sizes are subjected to a lift force acting in opposite directions.

Another aspect of the lift model is that the results obtained using Equation 13 show a gas bubble radial distribution that peaks at the wall, due to the high continuous phase velocity gradient. The predicted accumulation is abnormal and not reflected by experimental findings. In order to handle this problem, a lift force damping model is usually employed. In the lift damping model, the lift coefficient is multiplied by a limiter, λ_β, which can be calculated using the following expression:

$$\lambda_\beta = \frac{1}{2}\left(1 - \cos\left(\pi \min\left(\frac{y_w}{1.5 d_\beta}, 1\right)\right)\right), \quad (14)$$

where y_w is the distance from the center of the cell (here, the model is formulated for a finite-volume discretization) to the nearest wall. Once the distance is smaller than 1.5 times the bubble diameter, the limiter gradually decreases to zero.

Another way to handle this problem is to include the wall lubrication force, which tends to push the secondary phase away from the walls. In bubbly upward flows in a vertical pipe, this force results in the disperse phase concentrating in a region near, but not immediately adjacent, to the wall. It is calculated as follows:

$$\mathbf{A}_{\beta,\text{wall}} = C_w \rho_c \alpha_\beta |\mathbf{U}_c - \mathbf{V}_\beta|^2 \mathbf{n}, \quad (15)$$

where $\mathbf{n}$ is the unit normal pointing away from the wall and C_w is the wall lubrication coefficient, which can be calculated using different models. Readers should refer to the work of Hosokawa et al[5] and Antal et al[6] for more information.

The bubble pressure force acts as a driving force for bubbles to move from areas with higher phase fractions to areas of lower phase fraction. It arises due to the pressure variations in the continuous phase that are not resolved at the mesoscale. The bubble pressure force is defined by [48]

$$\mathbf{A}_{\beta,\text{bubblePres}} = \nabla\left(C_{bp}\rho_c \alpha_\beta (\mathbf{V}_\beta - \mathbf{U}_c)(\mathbf{V}_\beta - \mathbf{U}_c)\right), \quad (16)$$

where C_{bp} is the bubble pressure coefficient. The effect of the bubble pressure force in the QBMM is similar to that of the turbulent dispersion force in the macroscale model. These forces can ensure that the equation system is conditionally hyperbolic, which facilitates stabilization of the bubbly flow regime.[4]

Substituting all the forces in Equation 10, the velocity for the disperse phase of size d_β can be calculated. Because the drag force is important, the drag force term is treated implicitly, while other forces are treated explicitly. When the Euler-implicit time scheme is employed to solve the Equation 10, the velocities for the next time can be written as

$$\mathbf{V}_{\beta}^{t+\Delta t} = \frac{\mathbf{V}_{\beta}^{t} + \Delta t(S_p \mathbf{U}_c + S_u)}{1.0 + S_p \Delta t}, \tag{17}$$

$$S_u = \frac{w_{d_\beta}}{\alpha_{d_\beta}}\left(\mathbf{A}_{d_\beta,\text{buo}} + \mathbf{A}_{d_\beta,\text{lift}} + \mathbf{A}_{d_\beta,\text{wall}} + \mathbf{A}_{d_\beta,\text{bubblePres}}\right), S_p = \frac{3}{4}\frac{\alpha_\beta C_{D,\beta}\rho_c}{\rho_\beta d_\beta}. \tag{18}$$

Once the $\mathbf{V}_{\beta}^{t+\Delta t}$ have been updated, the mixed moments can be updated in terms of their definition as reported in Equation 8. Readers interested in details of the second step of the operator splitting procedure are invited to read our previous work.[40] At last, we finalize the discussion of the numerics of the E-QBMM and the E–E method by Table 2, in which the difference between the E-QBMM and the E–E method is summarized.

2.3 | Coupling and numerical discretization

From the initial settings, the disperse phase fraction can be calculated (e.g., $\alpha_d = \frac{\pi}{6} m_{0,0,0,3}$). Neglecting the shared pressure gradient force, lift force, wall lubrication force, bubble pressure force and the contribution of the disperse phase in the drag force, the semidiscretised form of the continuous phase momentum equation is

$$a_P\left(\mathbf{U}_{c,P}^{*} - \mathbf{U}_{c,P}^{0}\right) + \sum_N a_N \mathbf{U}_N = -\text{Sp}\mathbf{U}_{c,P}, \tag{19}$$

where a_P and a_N are the matrix diagonal and nondiagonal coefficients, which are a function of $\mathbf{U}_c$; $\mathbf{U}_{c,\,P,}$ and $\mathbf{U}_{c,\,N}$ are the unknown velocity of the continuous phase defined at and near the cell center. The solution of Equation 18 is the predicted continuous phase velocity, $\mathbf{U}_{c,P}^{*}$, defined by

$$\mathbf{U}_{c,P}^{*} = \frac{1}{a_P}\left(-\text{Sp}\mathbf{U}_{c,P} - \sum_N a_N \mathbf{U}_N + a_P \mathbf{U}_{c,P}^{0}\right). \tag{20}$$

The nondrag forces together with the contribution of the disperse phase in the drag force are defined as the momentum flux, $\phi_{c,\,\text{force},\,f}$:

$$\phi_{c,\text{force},f} = \frac{\left(\frac{S_p \mathbf{V}_\beta}{\rho_c} - \sum_{d_\beta=1}^{N} \alpha_\beta w_\beta \mathbf{A}_{\beta,\text{lift}} + \mathbf{A}_{\beta,\text{wall}} + \mathbf{A}_{\beta,\text{bubblePres}}\right)_f}{a_{P,f}} \cdot \mathbf{S}_f, \tag{21}$$

where $N_{d\beta}$ is the number of abscissas, $\mathbf{S}_f$ is the surface-normal vector, and f denotes the variables defined at cell faces. Substituting these into Equation 1 leads to the semi-discretised form:

$$\frac{\partial(\alpha_c \rho_c)}{\partial t} + \sum_N \left(\alpha_{c,f}\left(\mathbf{U}_{c,f}^{*} \cdot \mathbf{S}_f + \phi_{c,\text{force},f}\right)\right) = \sum \left(\nabla \frac{\alpha_{c,f}^2}{a_{P,f}} p_{P,f}\right) \cdot \mathbf{S}_f. \tag{22}$$

Once the pressure is computed from Equation 21, the corrected continuous phase velocity can be computed by the flux reconstruction in the PISO procedure.

2.4 | Turbulence model

The Reynolds stress arises in the momentum equations as a result of the averaging process. Different turbulence models can be employed to calculate the Reynolds stress, such as the k - ε model,[1] k - ω model,[49] or the k - ω SST model.[50] It was shown that the k - ω turbulence model yielded a better qualitative prediction of the bubble plume than the k - ε model, due to the low Reynolds number treatment of the former model.[49] Some other works show that the k - ε model can still yield good results in bubbly flows.[51,52] In this study, a two-phase k - ε model was employed. The equations are omitted for brevity and readers are refereed to other works for more details.[53] It should be noted that in general the bubble-induced turbulence (BIT) plays an important role. The presence of bubbles modifies the structure of the liquid turbulence field and the production of shear-induced turbulence, which in turns modifies the bubble distribution and the break-up and coalescence processes. These bubbles act as a source of the BIT, also generating turbulence in flows that would otherwise be laminar. In general, the BIT model includes a source term in the turbulence transport equations to account for the turbulence generated by the bubbles, and different models have been developed.[54-57] However, because BIT may not play a major role in the flows considered here, it neglected in this work.

3 | TEST CASES AND RESULTS

3.1 | Numerical configurations

The E-QBMM algorithm with the nondrag forces was implemented in the open-source CFD code OpenFOAM-5.x, which is based on the cell-centered finite-volume method. The solver is called twoWayGPBEFoam.[40] It employs a pressure-based solution algorithm designed for a colocated grid arrangement. The contribution of the large body forces (e.g., the buoyant force, the lift force) are treated as

TABLE 2 Summary of the two numerical approaches

	E-QBMM	Two-phase E–E
Continuous phase	Navier–stokes equation	Navier–stokes equation
Disperse phase	Moment transport equations with VPA.	Navier–stokes equation.
	Advantages: Bubbles of different sizes are transported at different velocities.	Advantages: Demands low computational resources.
	Disadvantages: Computationally demanding realizable finite-volume scheme should be employed.	Disadvantages: Bubbles of different sizes are transported at identical velocity.

momentum flux instead of source terms.[58] The higher order flux-splitting realizable scheme is implemented for the moment transport equations [44] with a MIN-MOD limiter.[59] The flux-corrected transport (FCT) scheme with a multidimensional universal limiter with explicit solution (MULES) is employed for the phase fraction equation to ensure the boundedness of the phase fraction.[60] The coupling of the shared pressure and the continuous phase velocity is solved by the PISO procedure.[61] The adiabatic solver reacting TwoPhaseEulerFoam without mass-transfer was also employed as a baseline solver in which the E–E method is implemented.

All the grids in the following test cases are generated by blockMesh. The mesh size is selected according to a grid independence study considering several factors, that is, achieving grid independent results, the capability of capturing profile near the wall. In the square channel test case studied by Žun,[41] a 2-D fully orthogonal non-uniform hexahedral grid with 25 (width) × 150 (height) × 1 (depth) cells was generated. In the cylinder pipe test case examined by Lucas et al [42] and Banowski et al,[29] 2.5-D fully orthogonal grids with 25 (width) × 410 (height) and 25 (width) × 200 (height) were generated, respectively. The mesh size is selected according to a grid independence study considering several factors, that is, achieving grid-independent results, the capability of capturing profile near the wall. It was shown in our preliminary investigations that such meshes achieve mesh-independent solutions. Mesh with higher resolution did not improve the predictions. The initial moments at the inlet are calculated by assuming a log-normal distribution.[62] The discretization scheme, sparse matrix solver, momentum closure models, and other details of these different test cases are listed in Tables 3–5. Since we employ the PISO algorithm, the pressure is solved iteratively at each time step. The relevant tolerance and the final tolerance equal 0.01 and 1×10^{-7}, respectively. Other variables (e.g., k and ε) are solved after the pressure and velocity iteration procedure, and the tolerance equals 1×10^{-7}. Since the moment transported equations are solved using the explicitly realizable scheme, a diagonal solver can be constructed and a relatively low tolerance (1×10^{-15}) is used. In order to minimize the time discretization error and to ensure the moments realizability, the time step is adjusted to ensure that the Courant number is smaller than 0.05. Unless otherwise stated, all the other simulations in the following sections are performed with identical settings.

It should be noted that the bubble diameter, phase fraction, and the velocity at the inlet work critically. Generally, the inlet disperse phase fraction and the bubble velocity are unknown except for the test case studied by Banowski et al.[29] The inlet velocity can be calculated from the superficial velocity using the following expression:

$$\mathbf{V}_{\text{inlet}} = \frac{\mathbf{V}_{\text{super}} \cdot \text{OutletArea}}{\text{inletArea} \cdot \alpha_{\text{inlet}}}. \tag{23}$$

A typical approach is to assume that the inlet bubble velocity equals the bubble terminal velocity, namely $\mathbf{V}_{\text{super}} = \mathbf{V}_{\text{TerminalV}}$; then, the inlet disperse phase fraction can be calculated. As is known, the single isolated gas bubble's terminal velocity in a liquid depends on buoyancy and drag force. Therefore, the bubble terminal velocity can be calculated from the balance between these forces, which requires the introduction of a drag model. On the other hand, a much simpler way is to use the existing model to calculate the bubble terminal velocity. For example, Davies and Taylor used the following expression to calculate the bubble terminal velocity:

$$|\mathbf{V}_{\text{TerminalV}}| = 0.707\sqrt{|\mathbf{g}|\,d}. \tag{24}$$

In this work, we employ another approach for all the test cases due to its simplicity. In this method, the inlet phase fraction is fixed at 0.5, and then the inlet bubble velocity satisfying the superficial velocity condition is calculated. It was found in our preliminary investigation that there is no difference between these methods.

TABLE 3 Numerical configurations used in the test cases

Term	Configuration
$\partial/\partial t$	Euler implicit
$\nabla\psi$	cellMDLimited leastSquares 1
∇p	Gauss linear
$\nabla \cdot (\psi\mathbf{UU})$	Gauss limitedLinearV 1;
$\nabla \cdot (\mathbf{U}\psi)$	Gauss limitedLinear 1
$\nabla \cdot \tau$	Gauss linear
$\nabla^2\psi$	Gauss linear uncorrected
$\nabla^{\perp}\psi$	Uncorrected
ψ_f	Linear
$w_{d\beta,f}$	MIN-MOD limiter
$d_{d\beta,f}$	Upwind

Note: ψ denotes a generic variable; $(\ldots)_f$ is the face interpolation operator; $\nabla^{\perp}$ is the surface-normal gradient. The number "1" indicates the compliance of the scheme with the definition of TVD scheme. A value of 1 indicates full TVD compliance.

3.2 | Test case studied by Žun

In this section, the experimental data of bubbly flows in a square channel investigated by Žun [41] was employed as a benchmark. The gas volume fraction profile was measured with microresistivity probes with a tip diameter of 0.011 mm, in a square-section channel, 0.0254 m inside for a liquid superficial velocity of 0.43 m/s. Before the simulation results were compared with the experimental data, simulation results predicted by the E-QBMM with a first-order scheme and higher order scheme were compared with those predicted by the

TABLE 4 Solvers and related settings used in the test cases

	Solver	Preconditioner	Rel. tol.	Final tol.
p	PCG	DIC	0.01	1e-7
k	PBiCGStab	DILU	-	1e-7
ε	PBiCGStab	DILU	-	1e-7
$m_{j,k,l,i}$	Diagonal	-	-	1e-15

TABLE 5 Momentum closure models and the test case details investigated in this work

	Test case of Žun [41]	Test case of Lucas et al [42]	Test case of Banowski et al [29]
Drag model	Schiller and Naumann [63]	Grace et al [64]	Grace et al [64]
Lift model	Tomiyama et al [27]	Tomiyama et al [27]	Tomiyama et al [27]
Wall model	Hosokawa et al [5]	Hosokawa et al [5]	Hosokawa et al [5]
Turbulent dispersion model	Biesheuvel et al [48]	Biesheuvel et al [48]	Biesheuvel et al [48]
Geometry	Square channel	Cylindrical pipe	Cylindrical pipe
Measurements available	α distribution	α distribution liquid velocity	α distribution
Features	Wall peak (mono-disperse) Double peak (poly-disperse)	Wall peak (mono-disperse)	Double peak (poly-disperse)
Sparger openings	Two separated single nozzles (exp)	Six separated single nozzles (exp)	Cylindrical ring with 16 holes (exp)

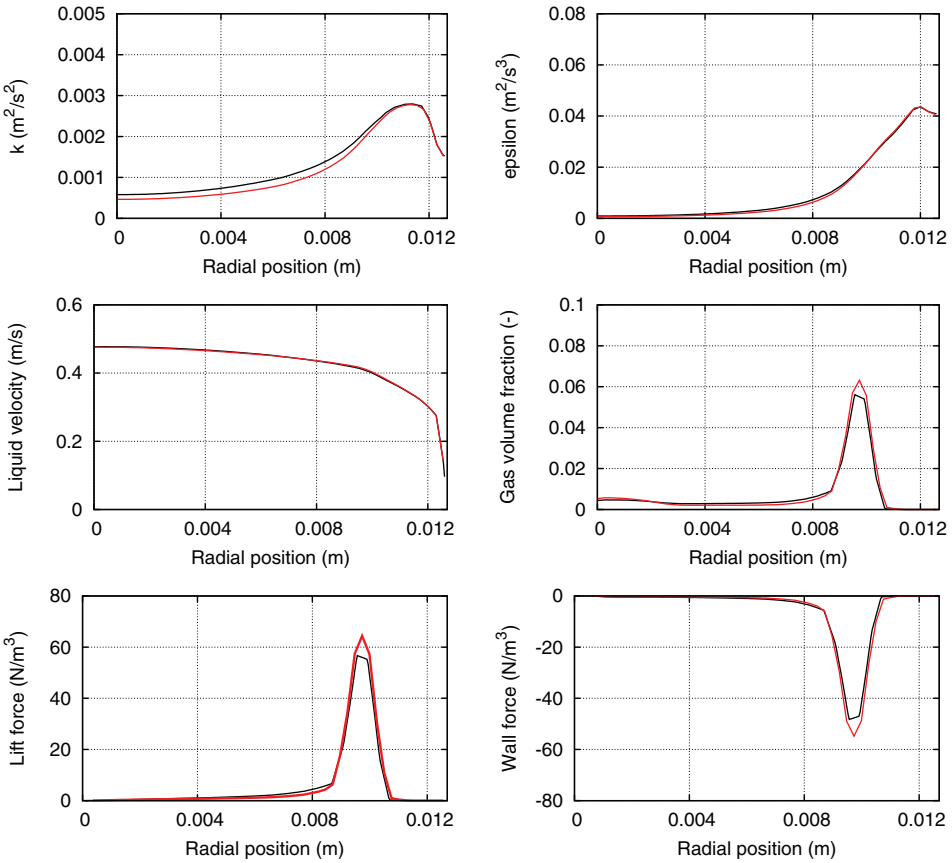

FIGURE 2 From top left to bottom right: Comparison of the turbulent kinetic energy, the turbulent energy dissipation rate, the liquid velocity, the phase fraction, the lift force, and the wall force by the E–E method (red line) and higher order E-QBMM (black line). Superficial velocity: 0.5 m/s. Liquid velocity: 0.43 m/s [Color figure can be viewed at wileyonlinelibrary.com]

E–E method in order to verify the E-QBMM algorithm and the wall forces implementations. The superficial gas velocity was set at 0.5 m/s. In the E–E method, the bubble size (constant in time and uniform in the computational domain) was set at 4 mm. In the E-QBMM, the value of the abscissas (bubble size) was also assumed to be identical (4 mm ± 1% in the case of singular problem in the moments inversion algorithm) with different weight values, meaning that it can be seen as a monodisperse system.

Figures 2 and 3 show the plots of the phase fraction, liquid velocity, turbulent kinetic energy, turbulent energy dissipation rate, lift force, and the wall lubrication force predicted by the E–E method and the E-QBMM by the higher order scheme and first-order scheme at L = 1.9 m, respectively. In these simulations, the drag force, lift force, and wall lubrication force are identical. Therefore, the results should be same. It can be seen that all the flow variables predicted by the E–E method and the higher order E-QBMM agree well with each other, which implies that the drag force, lift force, and wall lubrication force in the E-QBMM were implemented correctly. The phase fraction of the disperse phase and relevant variables (e.g., the lift force and wall force) predicted by the first-order two-way coupled E-QBMM are very diffusive due to the first-order spatial discretization scheme. Similar results can be also found in our previous work in which the one-way coupled E-QBMM was employed to simulate particle-size segregation.[40] The diffusive feature of the first-order spatial scheme can smash the wall peak phase fraction profile into vertical upward bubbly flows. The continuous phase variables (e.g., the liquid velocity

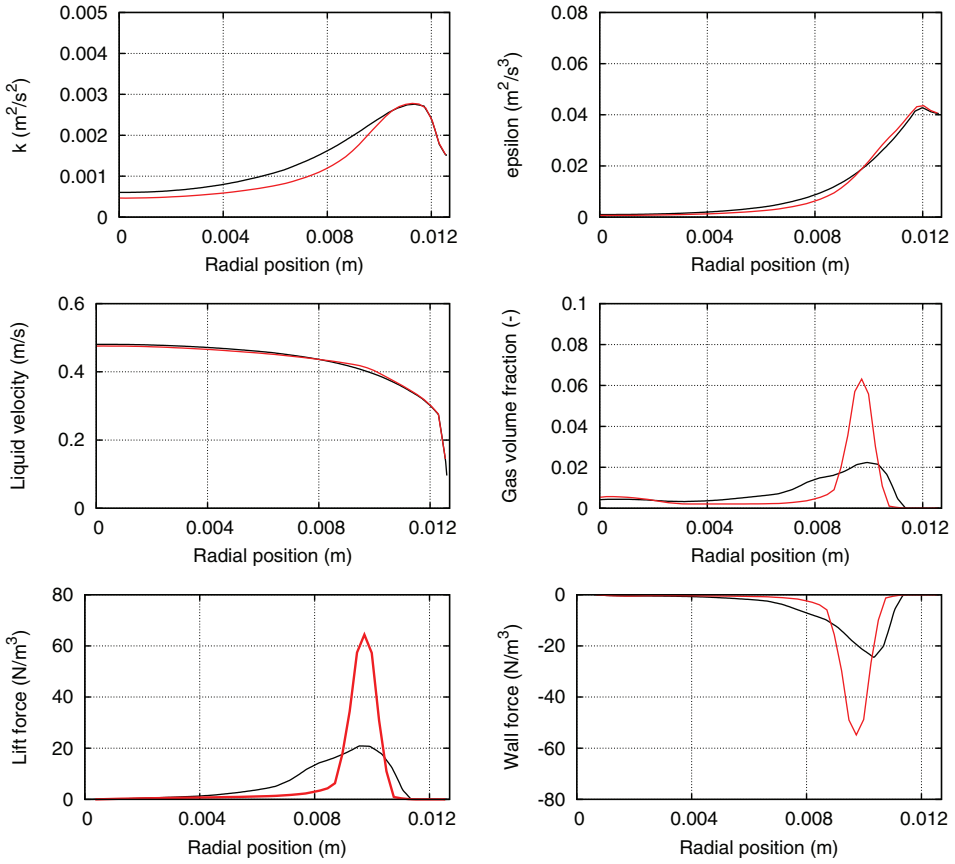

FIGURE 3 From top left to bottom right: Comparison of the turbulent kinetic energy, the turbulent energy dissipation rate, the liquid velocity, the phase fraction, the lift force, and the wall force by the E–E method (red line) and first-order E-QBMM (black line). Superficial velocity: 0.5 m/s. Liquid velocity: 0.43 m/s [Color figure can be viewed at wileyonlinelibrary.com]

TABLE 6 Prediction of the local liquid velocities by the E–E method and E-QBMM at different points

Radical location	Local liquid velocities	Local liquid velocities
(y = 1 m,z = 0 m)	Predicted by the E-QBMM	Predicted by the E–E method
Point 1 (x = 0 m)	0.449 m/s	0.463 m/s
Point 2 (x = 0.005 m)	0.448 m/s	0.449 m/s
Point 3 (x = 0.012 m)	0.347 m/s	0.346 m/s

and the turbulent kinetic energy) predicted by the first-order and higher order two-way coupled E-QBMM show no substantial difference, which implies that the spatial scheme of the disperse phase has little effect on the continuous phase. Therefore, in the following sections, all the test cases predicted by the E-QBMM were launched by the higher order spatial schemes.

Since the bubble size was assumed to be 4 mm, the wall peak was successfully predicted by the E-QBMM and the E–E method due to the lateral lift force and wall lubrication force, as shown in Figures 2 and 3. Moreover, the phase fraction in the vicinity of the wall decreases sharply because the lateral wall lubrication force pushes the bubbles away from it. As the bubble pressure force and the turbulent dispersion force are not included in the E-QBMM and the E–E method, the wall peaks predicted by both methods are rather strong, but still consistent with one other. The predictions of the turbulent kinetic energy and the turbulent energy dissipation rate also show the typical wall peak trend in bubbly flows, which is consistent with other works.[28,65] To further validate the algorithm, three points were selected to monitor the local liquid velocities predicted by the E-QBMM and the E–E method. It can be seen in Table 6 that the local liquid velocities predicted by these two different methods agree well with each other, which further implies that the implementation is correct.

To validate the turbulent dispersion force and the bubble pressure gradient force, the simulation results predicted by the E-QBMM and the E–E method were compared against measured data. The constant and uniform bubble size (abscissas value) was assumed to be 4.1 mm. As the author did not report the superficial gas velocity, it was assumed to be 0.5 m/s after a fitting procedure. A similar procedure can also be found in other works.[65] The turbulent dispersion force model proposed by reference 66, and the coefficient of the bubble pressure gradient force were assumed to be 2.0.[39] The predictions of the phase fraction by the E–E method and the E-QBMM at L/D = 45 are illustrated in Figure 4. It can be seen that both methods capture the wall peak, and the results predicted by both methods agree well with the experimental data. The sharp phase fraction profile reported in Figure 2 is flattened due to the existence of the turbulent dispersion force in the E–E method and the bubble pressure force in the E-QBMM. However, the predictions of the phase fraction by the E-QBMM and E–E method are underestimated near the wall. This is due to the overprediction of the wall lubrication model and can be improved by adjusting the wall lubrication force parameter. The predictions of the magnitude of the lift force and wall force by the E-QBMM and the E–E method are reported in Figure 5. These forces

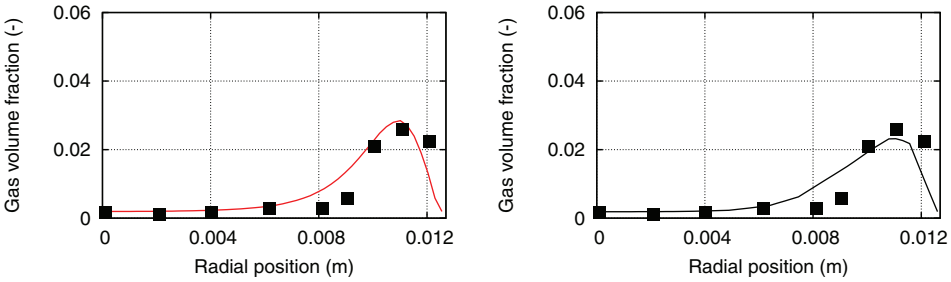

FIGURE 4 Comparison of the phase fraction predicted by the E–E method (left, black line) and E-QBMM (right, black line) with experimental data (dots). Superficial velocity: 0.5 m/s. Liquid velocity: 0.43 m/s [Color figure can be viewed at wileyonlinelibrary.com]

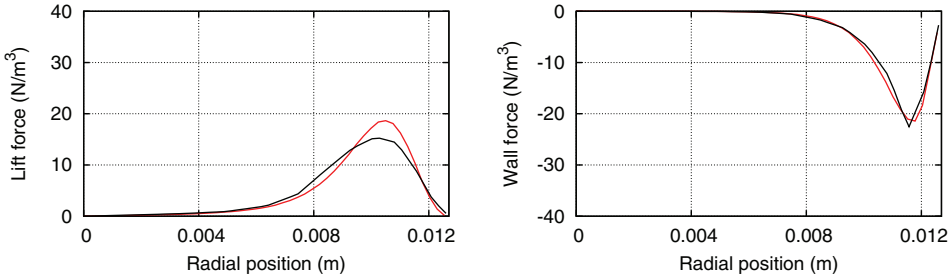

FIGURE 5 Comparison of the lift force (left) and wall force (right) predicted by the E–E method (red line) and the E-QBMM (black line). Homogeneous bubble size: 4 mm. Superficial velocity: 0.5 m/s. Liquid velocity: 0.43 m/s [Color figure can be viewed at wileyonlinelibrary.com]

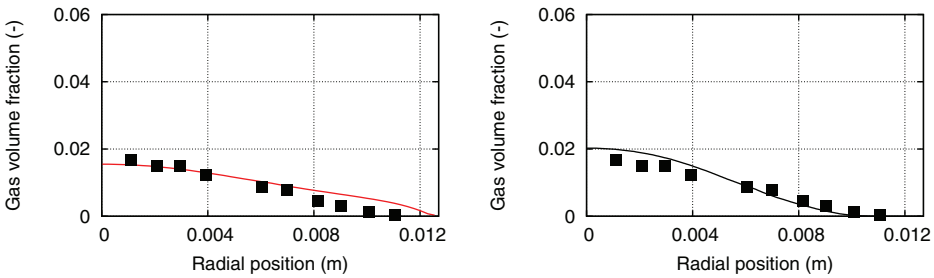

FIGURE 6 Comparison of the phase fraction predicted by the E–E method (left, black line) and E-QBMM (right, black line) with experimental data (dots). Homogeneous bubble size: 6.4 mm. Superficial velocity: 0.5 m/s. Liquid velocity: 0.43 m/s [Color figure can be viewed at wileyonlinelibrary.com]

reach a maximum value near the wall due to the large velocity gradient of the continuous phase and decrease to zero when the damping model is applied, as reported in Equation 14.

Next, the bubble size was assumed to be 6.4 mm, a value which is consistent with the experimental data in the work by Žun.[41] Other operating conditions are identical with previous ones. In experiments, these large bubbles should move to the pipe center in upward bubbly flows due to the negative lift force. Figure 6 shows the phase fraction predicted by the E-QBMM and the E–E method. In experiments, the bubbles tend to move toward the pipe center, and the nonuniform phase fraction distribution has the largest value at the pipe center. It can be seen that the phase fraction predicted by the E-QBMM, and the E–E method agree well with the experimental data due to the lift force predicted by the model developed by Tomiyama et al [27] with a negative coefficient.

Finally, the E-QBMM and E–E were employed to predict the evolution of polydisperse bubbly flows. In the E-QBMM simulation, the values of the abscissas were assumed to be 4 mm, 5.4 mm, and 6.5 mm, and weights' value were assumed to be 59,333, 48,559 and 32,423. In the E–E simulation, the bubble diameter equal to 5.44 mm, which is identical with the mean Sauter diameter in the E-QBMM. Other settings are identical with previous cases. These bubbles can be seen as three disperse phases with the same physical attributes (e.g., density) but different sizes. Since the sizes of the bubbles are different, the phase fraction profile should represent a phase segregation because the large bubbles move toward the center and small ones move toward the wall. In experiments, a double peak is captured and the simulation should be able to predict it. Since the abscissas' and weights' values are fixed, the moments are calculated by $m_{0,0,0,i} = \sum_{\beta=1}^{N} w_\beta d_\beta^i$. These moments are used as the initial inlet boundary condition values.

It can be seen in Figure 7 that the double peak phase fraction profile predicted by the E-QBMM agrees well with the experimental data. Moreover, Figure 8 shows the small bubbles and large bubbles predicted by the E-QBMM move in opposite directions since they are transported at their own velocities as seen in Equation 4. Meanwhile, it can be seen that a double peak of this type can never be predicted by the two-phase E–E method since only one bubble size can be fed into the mathematical models. It is possible to employ a three-phase E–E–E model (multi-fluid model) to predict a double peak, in which multiple momentum equations are employed for different phases of different sizes. The multifluid model resembles the three-phase E-QBMM-QBMM, in which two GPBEs are employed for the disperse phase. However, we would like to stress that the advantage of the E-QBMM over the E–E method is that even only one GPBE is employed for the polydisperse phase, the phase segregation can be successfully predicted by the E-QBMM.

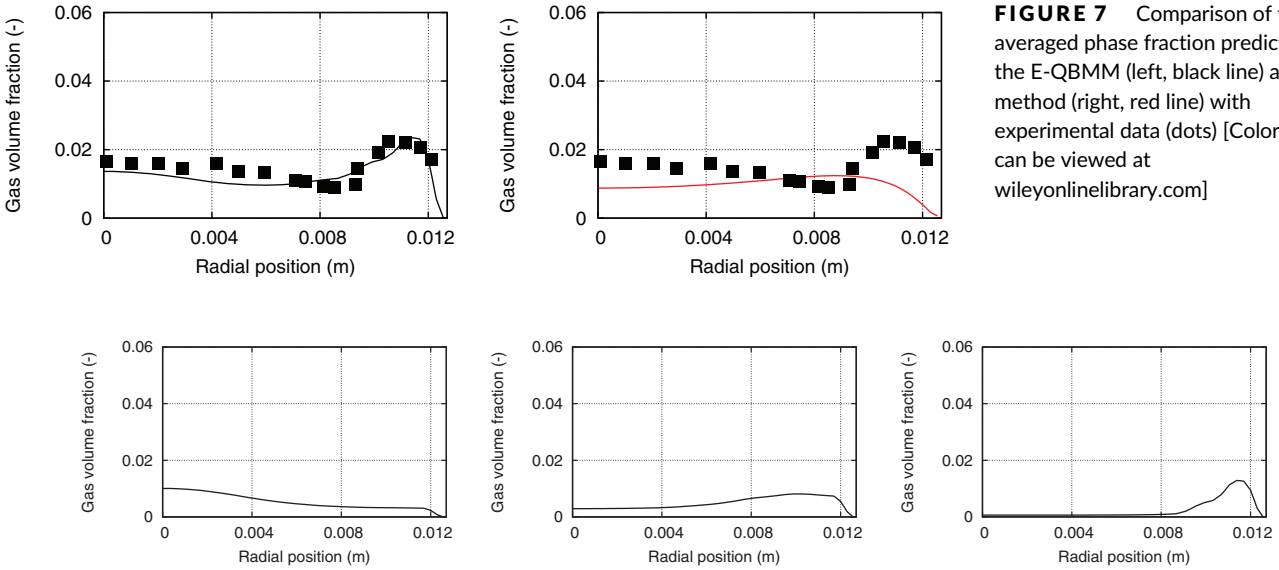

FIGURE 7 Comparison of the averaged phase fraction predicted by the E-QBMM (left, black line) and E–E method (right, red line) with experimental data (dots) [Color figure can be viewed at wileyonlinelibrary.com]

FIGURE 8 Comparison of the averaged phase fraction predicted by the E-QBMM for large (left), medium (middle), and small bubbles (right). Superficial velocity: 0.5 m/s. Liquid velocity: 0.43 m/s

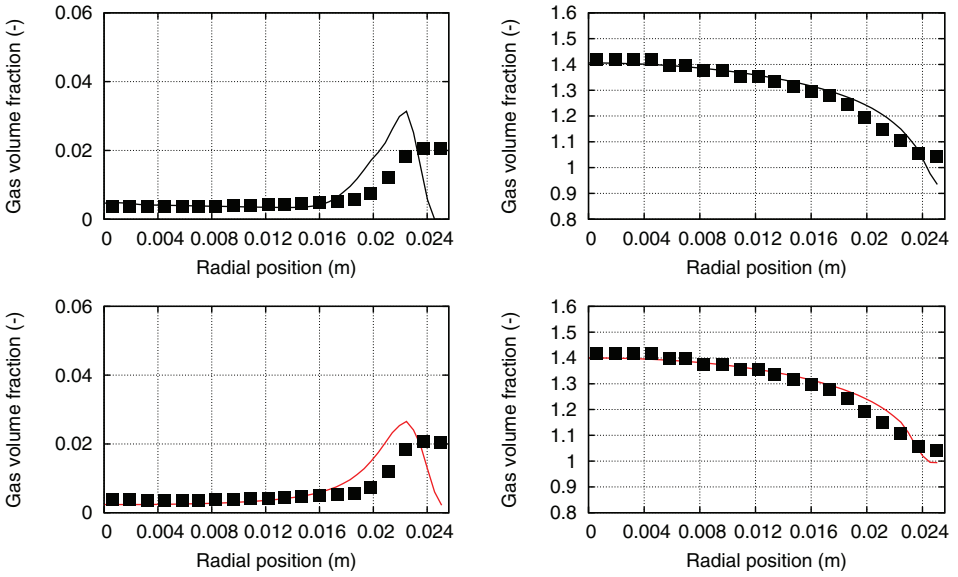

FIGURE 9 Comparison of the phase fraction (left) and the gas velocities (right) predicted by the E-QBMM (top, black line) and the E–E method (bottom, black line) with experimental data (dots). Monodisperse bubble size: 4.8 mm. Superficial velocity: 0.0096 m/s. Liquid velocity: 1.0167 m/s [Color figure can be viewed at wileyonlinelibrary.com]

3.3 | Test case studied by Lucas et al

The experimental data by Lucas et al [42] provide an opportunity to test the model against gas velocity data. The evolution of the bubbly flow was studied in a vertical tube with an inner diameter of 51.2 mm that was supplied with an air-water mixture. The vertical test section has a maximum length of about 4 m. In simulations, a wedge mesh was generated as discussed in Section 3.1. It is a typical mesh configuration and can save considerable computational resources.[67] The inlet turbulence intensity is assumed to be 5%, and the integral turbulent length scale is set to 10% of the pipe diameter. Varying this value had no discernible effect on the simulation results. The wall lubrication model developed by Hosokawa et al [5] was employed for this test case.

Figure 9 shows the phase fraction and the gas phase velocity predicted by the E-QBMM and the E–E method. It can be seen that the phase fraction predicted by the E-QBMM and the E–E method agree well with the experimental data. However, the right tail of the phase fraction plot predicted by both methods in the vicinity of the wall is lower than the experimental value. The reason for this slight underestimation is the overprediction of the wall lubrication forces near the wall. The gas velocities predicted by the E-QBMM and E–E agree well with measured data. Moreover, the velocities of the bubbles of identical sizes (≈4.8 mm) predicted by the E-QBMM overlap and agree well with experimental data, which implies that the algorithm and implementation are correct. Last but not least, it can be seen that the E-QBMM can also be employed to predict monodisperse multiphase systems.

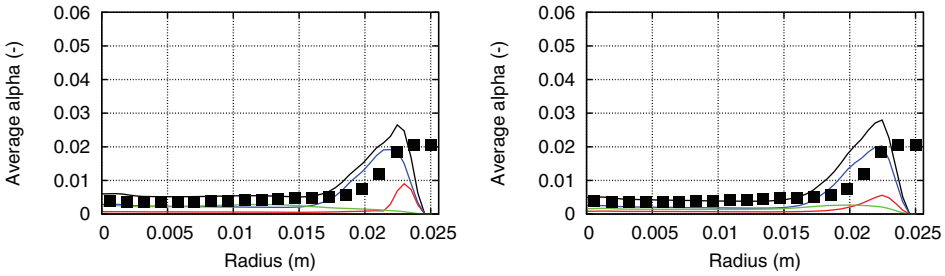

FIGURE 10 Comparison of the phase fraction predicted by the E-QBMM with experimental data (dots). Poly-disperse bubble sizes: 4.1/4.9/5.8 mm (left) and 4.3/4.9/5.6 mm (right). Black line: Averaged phases fraction. Red line: Contribution by small bubbles. Blue line: Contribution by medium bubbles. Green line: Contribution by large bubbles. Superficial velocity: 0.0096 m/s. Liquid velocity: 1.0167 m/s [Color figure can be viewed at wileyonlinelibrary.com]

FIGURE 11 Comparison of the phase fraction predicted by the E–E method (left, black line) and the E-QBMM (right, black line) with experimental data (dots). Superficial velocity: 0.0151 m/s. Liquid velocity: 1.017 m/s [Color figure can be viewed at wileyonlinelibrary.com]

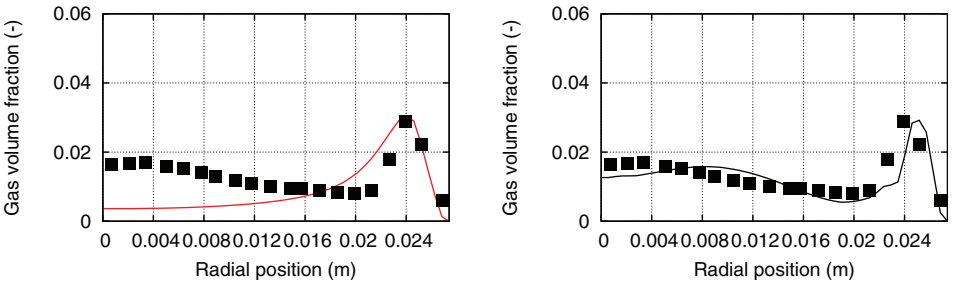

FIGURE 12 The contour plots of the developed phase fraction predicted by the E-QBMM at z = 0.01 m (top left), z = 0.1 m (top right), z = 1 m (bottom left), and z = 1.6 m (bottom right). Superficial velocity: 0.0151 m/s. Liquid velocity: 1.017 m/s [Color figure can be viewed at wileyonlinelibrary.com]

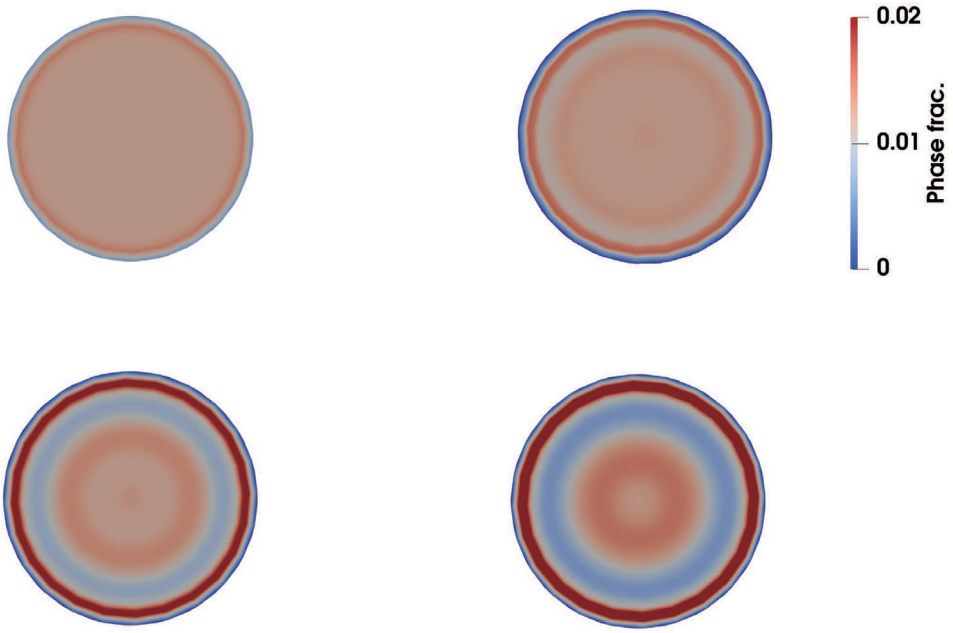

Now it is interesting to employ the E-QBMM to simulate a poly-disperse system by adjusting the bubble sizes. Figure 10 represents the phase fraction predicted by the E-QBMM for bubble sizes of 4.1/4.9/5.8 mm and 4.3/4.9/5.6 mm. It can be seen that bubbles of size smaller than 5.5 mm tend to move toward the wall, but the maximum value of the phase fraction is located at different positions. The smaller the bubbles are, the closer they accumulate to the wall. On the other hand, the large bubbles (i.e., larger than 5.5 mm) tend to move toward the pipe center, which is consistent with the physics. Moreover, the overall phase fraction profile predicted by E-QBMM still represents a wall peak even in this polydisperse system since the mean Sauter diameter is smaller than 5.5 mm.

3.4 | Test case by Banowski et al

Finally, we complete the study with a relatively recent work by Banowski et al.[29] In that work, air/water two-phase co-current upward flows in a vertical pipe are investigated using X-ray tomography. The test section comprises a vertical titanium pipe with an inner diameter of 54.8 mm and a length of 6 m. Gas is injected into the

water stream at the bottom of the pipe 0.5 m downstream from the bend via an injection module with sparger rings. The superficial velocities of the air and water are 0.0151 and 1.017 m/s, respectively. The radial gas phase fraction is monitored at L/D = 59 for different bubble size classes.

The numerical configurations in the E-QBMM simulations are identical with previous test cases. The phase fraction predicted by the E-QBMM and the E–E method are reported in Figure 11. Again, it can be seen that the double peak was predicted by the E-QBMM due to large bubbles moving toward the pipe center and small bubbles moving toward the wall. The two-phase E–E method fails to predict the double peak since it is only applicable for monodisperse phase systems. A multiphase E–E method combined with the inhomogeneous MUSIG model should be able to handle the problem, in which multiple momentum equations are employed for the disperse phase.[34] However, in order to make a justified comparison with the E-QBMM, in which only one GPBE is employed for the disperse phase, only the two-phase E–E method is investigated in this work.

The contour plots of the phase fraction predicted by the E-QBMM and the E–E method at different horizontal sections are shown in Figure 12. It can be seen that the plots predicted by the E-QBMM also capture the double peak in vertical upward poly-disperse bubbly flows in upper sections. It should be noted that in our previous work,[40] we found that the flow field information (e.g., the phase fraction distribution) is highly dependent on the inlet conditions for a sudden-enlargement gas–liquid test case with a relatively low L/R value. However, even if a uniform phase fraction is given for the test case by Banowski et al, the phase fraction profile still develops gradually to nonuniform distribution along the vertical pipe direction. This implies that there is enough time for the phase fraction to develop in similar vertical upward bubbly flows with high L/R values.

4 | CONCLUSIONS

In this work, the higher order fully coupled E-QBMM with a full set of momentum interfacial exchange terms (e.g., the drag/lift/wall lubrication/bubble pressure forces) was implemented in open-source CFD code OpenFOAM-5.x, in which the conditioned disperse velocity is modeled by the VPA. The solver is called `twoWayGPBEFoam`, and it was employed to simulate monodisperse and polydisperse bubbly flows in vertical upward channels. `reactingTwoPhaseEulerFoam` was also employed as a benchmark model comparison, in which the E–E method is implemented. Different experimental data from different works featuring wall peaks and double peaks were selected to verify the algorithm and the implementations.

We show that the results predicted by the higher order E-QBMM are identical to those predicted by the E–E method. For bubbly flows, when the bubbles are small, both methods can predict the wall peak. For bubbly flows with large diameters, the predictions using both methods show the bubbles moving toward the channel/pipe center due to the negative lift force coefficient, which is consistent with experimental data. When large bubbles and small bubbles exist alongside one another, constituting a polydisperse system, the double peak can be successfully predicted by the E-QBMM, since the bubbles of different sizes are transported at different velocities (see Equation 4). Moreover, the bubble pressure force and turbulent dispersion force can smooth the lateral phase fraction distribution, and the overprediction of the wall lubrication force incurs an underestimation of the phase fraction in a small region in the vicinity of the wall. Improvements can be achieved by a more sophisticated combination of the nondrag forces and the breakage and coalescence model.

ACKNOWLEDGMENT

This work was partially supported by Helmholtz-Zentrum Dresden-Rossendorf. One author (Dongyue Li) wants to acknowledge the continued encouragement of the CFD-China community. Open access funding enabled and organized by Projekt DEAL.

ORCID

Dongyue Li https://orcid.org/0000-0001-5781-2366

REFERENCES

1. Krepper E, Lucas D, Prasser H. On the modelling of bubbly flow in vertical pipes. *Nuclear Eng Des*. 2005;235:597-611.
2. Hibiki T, Ishii M. Lift force in bubbly flow systems. *Chem Eng Sci*. 2007;62:6457-6474.
3. Rzehak R, Krepper E, Lifante C. Comparative study of wall-force models for the simulation of bubbly flows. *Nuclear Eng Des*. 2012;253:41-49.
4. Panicker N, Passalacqua A, Fox RO. On the hyperbolicity of the two-fluid model for gas–liquid bubbly flows. *Appl Mathem Model*. 2018;57:432-447.
5. Hosokawa S, Tomiyama A, Misaki S, Hamada T. Lateral migration of single bubbles due to the presence of wall. In *ASME 2002 Joint US-European Fluids Engineering Division Conference*. Montreal: American Society of Mechanical Engineers. https://proceedings.asmedigitalcollection.asme.org/proceeding.aspx?articleid=1577371
6. Antal SP, Lahey RT, Flaherty JE. Analysis of phase distribution in fully developed laminar bubbly two-phase. *Flow Int J Multiph Flow*. 1991;17:635-652.
7. Besagni G, Inzoli F. Comprehensive experimental investigation of counter-current bubble column hydrodynamics: holdup, flow regime transition, bubble size distributions and local flow properties. *Chem Eng Sci*. 2016;146:259-290.
8. Besagni G, Inzoli F. Influence of internals on counter-current bubble column hydrodynamics: holdup, flow regime transition and local flow properties. *Chem Eng Sci*. 2016;145:162-180.
9. Besagni G, Inzoli F, De Guido G, Pellegrini LA. The dual effect of viscosity on bubble column hydrodynamics. *Chem Eng Sci*. 2017;158:509-538.
10. Sasaki S, Uchida K, Hayashi K, Tomiyama A. Effects of column diameter and liquid height on gas holdup in air-water bubble columns. *Experim Thermal Fluid Sci*. 2017;82:359-366.
11. Colombo M, Fairweather M. Multiphase turbulence in bubbly flows: RANS simulations. *Int J Multiph Flow*. 2015;77:222-243.
12. Colombo M, Fairweather M. Accuracy of Eulerian–Eulerian, two-fluid CFD boiling models of subcooled boiling flows. *Int J Heat Mass Transfer*. 2016;103:28-44.

13. Li D, Christian H. Simulation of bubbly flows with special numerical treatments of the semi-conservative and fully conservative two-fluid model. *Chem Eng Sci*. 2017;174:25-39.
14. Shi P, Rzehak R. Bubbly flow in stirred tanks: Euler-Euler/RANS Modeling. *Chem Eng Sci*. 2018;190:419-435.
15. Besagni G, Inzoli F. The effect of electrolyte concentration on counter-current gas–liquid bubble column fluid dynamics: gas holdup, flow regime transition and bubble size distributions. *Chem Eng Res Des*. 2017;118:170-193.
16. Besagni G, Guédon G, Inzoli F. Computational fluid-dynamic modeling of the mono-dispersed homogeneous flow regime in bubble columns. *Nuclear Eng Des*. 2018;331:222-237.
17. Hecht KJ, Krause U, Hofinger J, Bey O, Nilles M, Renze P. Prediction of gas density effects on bubbly flow hydrodynamics: new insights through an approach combining population balance models and computational fluid dynamics. *AIChE J*. 2018;64:3764-3774.
18. Liao Y, Lucas D, Krepper E. Application of new closure models for bubble coalescence and breakup to steam–water vertical pipe flow. *Nucl Eng Des*. 2014;279:126-136.
19. Li D, Buffo A, Podgórska W, Gao Z, Marchisio DL. Droplet breakage and coalescence in liquid-liquid dispersions: comparison of different kernels with EQMOM and QMOM. *AIChE J*. 2017;63:2293-2311.
20. Li D, Buffo A, Podgórska W, Marchisio DL, Gao Z. Investigation of droplet breakup in liquid-liquid dispersions by CFD-PBM simulations: the influence of the surfactant type. *Chin J Chem Eng*. 2017;25:1369-1380.
21. Xie L, Liu Q, Luo Z. A multiscale CFD-PBM coupled model for the kinetics and liquid–liquid dispersion behavior in a suspension polymerization stirred tank. *Chem Eng Res Des*. 2018;130:1-17.
22. Vik C, Solsvik J, Hillestad M, Jakobsen HA. A multifluid-PBE model for simulation of mass transfer limited processes operated in bubble columns. *Comput Chem Eng*. 2018;110:115-139.
23. Chen C, Guan X, Ren Y, et al. Mesoscale modeling of emulsification in rotor-stator devices: part II: a model framework integrating emulsifier adsorption. *Chem Eng Sci*. 2019;193:156-170.
24. Chen C, Guan X, Ren Y, et al. Mesoscale modeling of emulsification in rotor-stator devices: part I: a population balance model based on EMMS concept. *Chem Eng Sci*. 2019;193:171-183.
25. Li D, Li Z, Gao Z. Quadrature-based moment methods for the population balance equation: an algorithm review. *Chin J Chem Eng*. 2019;27:483-500.
26. Gao Z, Li D, Buffo A, Podgórska W, Marchisio DL. Simulation of droplet breakage in turbulent liquid–liquid dispersions with CFD-PBM: comparison of breakage kernels. *Chem Eng Sci*. 2016;142:277-288.
27. Tomiyama A, Tamai H, Zun I, Hosokawa S. Transverse migration of single bubbles in simple shear flows. *Chem Eng Sci*. 2002;57:1849-1858.
28. Lucas D, Akio T. On the role of the lateral lift force in poly-dispersed bubbly flows. *Int J Multiphase Flow*. 2011;37:1178-1190.
29. Banowski M, Hampel U, Krepper E, Beyer M, Lucas D. Experimental investigation of two-phase pipe flow with ultrafast X-ray tomography and comparison with state-of-the-art CFD simulations. *Nucl Eng Des*. 2018;336:90-104.
30. McGraw R. Description of aerosol dynamics by the quadrature method of moments. *Aerosol Sci Tech*. 1997;27:255-265.
31. Lo S. Application of the MUSIG model to bubbly flows *AEAT-1096*. *AEA Technol*. 1996;230:8216-8246.
32. Dorao CA, Jakobsen HA. A least squares method for the solution of population balance problems. *Comput Chem Eng*. 2006;30:535-547.
33. Kumar S, Ramkrishna D. On the solution of population balance equations by discretization–I. A fixed pivot technique. *Chem Eng Sci*. 1996;51:1311-1332.
34. Krepper E, Lucas D, Frank T, Prasser H, Zwart P. The inhomogeneous MUSIG model for the simulation of polydispersed flows. *Nucl Eng Des*. 2008;238:1690-1702.
35. Lucas D, Rzehak R, Krepper E, et al. A strategy for the qualification of multi-fluid approaches for nuclear reactor safety. *Nucl Eng Des*. 2016;299:2-11.
36. Xiao Q, Wang J, Yang N, Li J. Simulation of the multiphase flow in bubble columns with stability-constrained multi-fluid CFD models. *Chem Eng J*. 2017;329:88-99.
37. Yuan C, Fox RO. Conditional quadrature method of moments for kinetic equations. *J Comput Phys*. 2011;230:8216-8246.
38. Marchisio DL, Fox RO. *Computational models for polydisperse particulate and multiphase systems*. Cambridge, UK: Cambridge University Press; 2013.
39. Yuan C, Kong B, Passalacqua A, Fox RO. An extended quadrature-based mass-velocity moment model for polydisperse bubbly flows. *Can J Chem Eng*. 2014;92:2053-2066.
40. Li D, Marchisio DL, Hasse C, Lucas D. twoWayGPBEFoam: an open-source Eulerian-QBMM solver for monokinetic bubbly flows. *Comput Phys Commun*. Submitted.
41. Žun I. The mechanism of bubble non-homogeneous distribution in two-phase shear flow. *Nucl Eng Des*. 1990;118:155-162.
42. Lucas D, Krepper E, Prasser HM. Development of co-current air–water flow in a vertical pipe. *Int J Multiph Flow*. 2005;31:1304-1328.
43. Wheeler JC. Modified moments and Gaussian quadratures. *Rocky Mountain J Mathem*. 1974;4:287-296.
44. Vikas V, Wang ZJ, Passalacqua A, Fox RO. Realizable high-order finite-volume schemes for quadrature-based moment methods. *J Computat Phys*. 2011;230:5328-5352.
45. Besagni G, Inzoli F. Bubble size distributions and shapes in annular gap bubble column. *Experim Thermal Fluid Sci*. 2016;74:27-48.
46. Wellek RM, Agrawal AK, Skelland AHP. Shape of liquid drops moving in liquid media. *AIChE J*. 1966;12:854-862.
47. Ziegenhein T, Tomiyama A, Lucas D. A new measuring concept to determine the lift force for distorted bubbles in low Morton number system: results for air/water. *Int J Multiph Flow*. 2018;108:11-24.
48. Biesheuvel A, Gorissen WCM. Void fraction disturbances in a uniform bubbly fluid. *Int J Multiph Flow*. 1990;16:211-231.
49. Bech K. Dynamic simulation of a 2D bubble column. *Chem Eng Sci*. 2005;60:5294-5304.
50. Besagni G, Inzoli F, Ziegenhein T, Lucas D. Computational fluid-dynamic modeling of the pseudo-homogeneous flow regime in large-scale bubble columns. *Chem Eng Sci*. 2017;160:144-160.
51. Sharma SL, Hibiki T, Ishii M, et al. An interfacial shear term evaluation study for adiabatic dispersed air–water two-phase flow with the two-fluid model using CFD. *Nucl Eng Des*. 2017;312:389-398.
52. Bhusare VH, Dhiman MK, Kalaga DV, Roy S, Joshi JB. CFD simulations of a bubble column with and without internals by using OpenFOAM. *Chem Eng J*. 2017;317:157-174.
53. Lahey RT. The simulation of multidimensional multiphase flows. *Nucl Eng Des*. 2005;235:1043-1060.
54. Sato Y, Sekoguchi K. Liquid velocity distribution in two-phase bubble flow. *Int J Multiph Flow*. 1975;2:79-95.
55. Lahey RT, Drew DA. The analysis of two-phase flow and heat transfer using a multidimensional, four field, two-fluid model. *Nucl Eng Des*. 2001;204:29-44.
56. Yao W, Morel C. Volumetric interfacial area prediction in upward bubbly two-phase flow. *Int J Heat Mass Trans*. 2004;47:307-328.
57. Ma T, Santarelli C, Ziegenhein T, Lucas D, Fröhlich J. Direct numerical simulation–based Reynolds-averaged closure for bubble-induced turbulence. *Phys Rev Fluids*. 2017;2:034301.
58. Zhang S, Zhao X, Bayyuk S. Generalized formulations for the Rhie-chow interpolation. *J Computat Phys*. 2014;258:880-914.
59. Van Leer B. Towards the ultimate conservative difference scheme. V. a second-order sequel to Godunov's method. *J Comput Phys*. 1979;32:101-136.

60. Boris JP, Book DL. Flux-corrected transport. I. SHASTA, a fluid transport algorithm that works. *J Comput Phys*. 1973;11:38-69.
61. Issa RI, Gosman AD, Watkins AP. The computation of compressible and incompressible recirculating flows by a non-iterative implicit scheme. *J Comput Phys*. 1986;62:66-82.
62. Petitti M, Vanni M, Marchisio DL, Buffo A, Podenzani F. Simulation of coalescence, break-up and mass transfer in a gas–liquid stirred tank with CQMOM. *Chem Eng J*. 2013;228:1182-1194.
63. Schiller L, Naumann A. A drag coefficient correlation *VDI*. *Zeitung*. 1935;77:51-86.
64. Grace JR, Wairegi T, Nguyen TH. Shapes and velocities of single drops and bubbles moving freely through immiscible liquids. *Chem Eng Res Des*. 1976;54:167-173.
65. Politano MS, Carrica PM, Converti J. A model for turbulent polydisperse two-phase flow in vertical channels. *Int J Multiph Flow*. 2003; 29:1153-1182.
66. Burns AD, Frank T, Hamill I, Shi JM The Favre averaged drag model for turbulent dispersion in Eulerian multi-phase flows in *5th international conference on multiphase flow*, *ICMF*;4:1–17 2004.
67. Rzehak R, Kriebitzsch S. Multiphase CFD-simulation of bubbly pipe flow: a code comparison. *Int J Multiph Flow*. 2015;68: 135-152.

How to cite this article: Li D, Marchisio D, Hasse C, Lucas D. Comparison of Eulerian QBMM and classical Eulerian–Eulerian method for the simulation of polydisperse bubbly flows. *AIChE J*. 2019;65:e16732. https://doi.org/10.1002/aic.16732